14. The CF occurs in the portion of the mid-IR spectrum where the real part of the complex refractive index is changing rapidly and approaching that of the surrounding medium, resulting in minimal scattering and an emissivity maximum.
15. Materials and methods are available as supporting material on *Science* Online.
16. P. D. Spudis, B. R. Hawke, P. Lucey, *J. Geophys. Res.* **89**, C197 (1984).
17. We defined a line using channels 3 and 5 and interpolated the value of the channel 4 emissivity on this line. We then subtracted the true channel-4 emissivity from this value.
18. M. Ohtake *et al.*, *Nature* **461**, 236 (2009).
19. Diviner data meeting our analysis criteria have not been acquired over Mons La Hire, Darney Chi, or Darney Tau.
20. P. G. Lucey, G. J. Taylor, E. Malaret, *Science* **268**, 1150 (1995).
21. P. G. Lucey, D. T. Blewett, B. R. Hawke, *J. Geophys. Res.* **103**, 3679 (1998).
22. B. R. Hawke *et al.*, *J. Geophys. Res.* **108**, 5069 (2003).
23. P. G. Lucey, B. R. Hawke, C. M. Pieters, J. W. Head, T. B. McCord, *J. Geophys. Res.* **91** (suppl.), D344 (1986).
24. B. B. Wilcox, P. G. Lucey, B. R. Hawke, *J. Geophys. Res.* **111**, E09001 (2006).
25. C. A. Wood, J. W. Head, *Conference on the Origin of Mare Basalts* (Lunar Science Institute, Houston, TX, 1975).
26. R. Wagner *et al.*, *Lunar Planet. Sci.* **XXVII**, 1367 (abstract) (1996).
27. L. E. Nyquist, C. Y. Shih, *Geochim. Cosmochim. Acta* **56**, 2213 (1992).
28. B. L. Jolliff *et al.*, *Am. Mineral.* **84**, 821 (1999).
29. C. R. Neal, L. A. Taylor, *Geochim. Cosmochim. Acta* **53**, 529 (1989).
30. B. L. Jolliff, *Int. Geol. Rev.* **40**, 916 (1998).
31. S. Maaløe, A. R. McBirney, *J. Volcanol. Geotherm. Res.* **76**, 111 (1997).
32. B. L. Jolliff, J. J. Gillis, L. A. Haskin, R. L. Korotev, M. A. Wieczorek, *J. Geophys. Res.* **105**, 4197 (2000).
33. D. J. Lawrence *et al.*, *J. Geophys. Res.* **105**, 20307 (2000).
34. This work was funded in part by the Diviner science budget. T.D.G., J.L.B., M.B.W., and R.C.E. were supported by the NASA Lunar Reconnaissance Orbiter Participating Scientist program.

Rainforest Aerosols as Biogenic Nuclei of Clouds and Precipitation in the Amazon

U. Pöschl,[1]* S. T. Martin,[2]* B. Sinha,[1] Q. Chen,[2] S. S. Gunthe,[1] J. A. Huffman,[1] S. Borrmann,[1] D. K. Farmer,[3] R. M. Garland,[1] G. Helas,[1] J. L. Jimenez,[3] S. M. King,[2] A. Manzi,[4] E. Mikhailov,[1,5] T. Pauliquevis,[6,7] M. D. Petters,[8,9] A. J. Prenni,[8] P. Roldin,[10] D. Rose,[1] J. Schneider,[1] H. Su,[1] S. R. Zorn,[1,2] P. Artaxo,[6] M. O. Andreae[1]

The Amazon is one of the few continental regions where atmospheric aerosol particles and their effects on climate are not dominated by anthropogenic sources. During the wet season, the ambient conditions approach those of the pristine pre-industrial era. We show that the fine submicrometer particles accounting for most cloud condensation nuclei are predominantly composed of secondary organic material formed by oxidation of gaseous biogenic precursors. Supermicrometer particles, which are relevant as ice nuclei, consist mostly of primary biological material directly released from rainforest biota. The Amazon Basin appears to be a biogeochemical reactor, in which the biosphere and atmospheric photochemistry produce nuclei for clouds and precipitation sustaining the hydrological cycle. The prevailing regime of aerosol-cloud interactions in this natural environment is distinctly different from polluted regions.

Atmospheric aerosols are key elements of the climate system. Depending on composition and abundance, aerosols can influence Earth's energy budget by scattering or absorbing radiation and can modify the characteristics of clouds and enhance or suppress precipitation. The direct and indirect aerosol effects on climate are among the largest uncertainties in the current understanding of regional and global environmental change. A crucial challenge is developing a quantitative understanding of the sources and properties of aerosol particles, including primary emission from the Earth's surface, secondary formation in the atmosphere, chemical composition and mixing state, and the ability to nucleate cloud droplets and ice crystals—all as influenced by human activities as compared with natural conditions (*1–4*).

During the wet season, the Amazon Basin is one of the few continental regions where aerosols can be studied under near-natural conditions (*5–7*). The Amazonian Aerosol Characterization Experiment 2008 (AMAZE-08) was conducted in the middle of the wet season at a remote site north of Manaus, Brazil (February to March 2008), and the investigated air masses came with the trade wind circulation from the northeast over some 1600 km of pristine tropical rainforest (*8*). Here, we focus on measurements performed in the period of 3 to 13 March 2008, when the influence of long-range transport from the Atlantic Ocean, Africa, or regional anthropogenic sources of pollution was particularly low and the aerosol properties were dominated by particles emitted or formed within the rainforest ecosystem (*6, 7, 9, 10*). The

measurement techniques applied include scanning electron microscopy (SEM) with energy-dispersive x-ray spectroscopy (EDX), atomic force microscopy (AFM), secondary ion mass spectrometry (NanoSIMS), aerosol mass spectrometry (AMS), differential mobility particle sizing (DMPS), ultraviolet aerodynamic particle sizing (UV-APS), and counting of cloud condensation nuclei (CCN) and ice nuclei (IN) (*8*). To our knowledge, this study provides the first comprehensive, detailed, and size-resolved account of the chemical composition, mixing state, CCN activity, and IN activity of particles in pristine rainforest air approximating pre-industrial conditions (*5–7*).

SEM images of characteristic particle types are shown in Fig. 1. Nearly all detected particles could be attributed to one of the following five categories: (i) secondary organic aerosol (SOA) droplets that were formed by atmospheric oxidation and gas-to-particle conversion of biogenic volatile organic compounds (*9*) and in which no other chemical components were detectable; (ii) SOA-inorganic particles composed of secondary organic material mixed with sulfates and/or chlorides from regional or marine sources (*6*); (iii) primary biological aerosol (PBA) particles, such as plant fragments or fungal spores (*6, 11, 12*); (iv) mineral dust particles consisting mostly of clay minerals from the Sahara desert (*6, 13*); or (v) pyrogenic carbon particles that exhibited characteristic agglomerate structures and originated from regional or African sources of biomass burning or fossil fuel combustion (*6*). In mixed SOA-inorganic particles, the organic fraction was typically larger than the inorganic fraction. The primary biological, mineral dust, and pyrogenic carbon particles were also partially coated with organic material [supporting online material (SOM) text].

The average number and mass size distribution, composition, and mixing state of particles as detected with microscopy and complementary online measurements are shown in Fig. 2. The online instruments measure different types of equivalent diameters, which can vary depending on the shape and the density of the particles. Nevertheless, the size distribution patterns obtained with the different techniques are in overall agreement with each other. SEM is the one method that cov-

[1]Max Planck Institute for Chemistry, 55128 Mainz, Germany. [2]School of Engineering and Applied Sciences and Department of Earth and Planetary Sciences, Harvard University, Cambridge, MA 02138, USA. [3]Department of Chemistry and Biochemistry and Cooperative Institute for Research in Environmental Science, University of Colorado, Boulder, CO 80309, USA. [4]National Institute of Amazonian Research, 69060 Manaus, Brazil. [5]Atmospheric Physics Department, Institute of Physics, St. Petersburg State University, 198904 St. Petersburg, Russia. [6]Institute of Physics, University of São Paulo, 05508 São Paulo, Brazil. [7]Federal University of São Paulo, 04023 Diadema, Brazil. [8]Department of Atmospheric Science, Colorado State University, Fort Collins, CO 80523, USA. [9]Marine Earth and Atmospheric Science, North Carolina State University, Raleigh, NC 27695, USA. [10]Department of Physics, Lund University, 22100 Lund, Sweden.

*To whom correspondence should be addressed. E-mail: u.poschl@mpic.de (U.P.); scot_martin@harvard.edu (S.T.M.)

ers the full particle size range and provides detailed information about composition and mixing state. The online measurement techniques, however, are more reliable for the absolute concentration values because of their better sampling and counting statistics. The integral particle number and mass concentrations as well as the relative proportions of different types of particles corresponding to the displayed size distributions are summarized in tables S1 and S2. The observed particle number and mass size distributions can be separated into two characteristic fractions with a dividing diameter of 1 μm. The submicrometer fraction dominated the total particle number concentration (>99% of ~200 cm^{-3}) (Fig. 2A and table S1), whereas the supermicrometer fraction accounted for most of the total particle mass concentration (~70% of ~2 μg m^{-3}) (Fig. 2C and table S2).

The submicrometer fraction exhibited three characteristic modes as indicated by local maxima in the number size distribution (Fig. 2B): a nucleation mode (<0.03 μm), an Aitken mode (0.03 to 0.1 μm), and an accumulation mode (0.1 to 1 μm). According to single particle analysis (SEM, AFM, and NanoSIMS), pure SOA droplets dominated the nucleation and Aitken modes (number fraction >99%) (Fig. 2A). The accumulation mode consisted of pure SOA droplets, mixed SOA-inorganic particles, and pyrogenic carbon particles. Overall, the pure SOA droplets represented ~85% of the number concentration of submicrometer particles and potential CCN, and the mixed SOA-inorganic particles accounted for another ~10% (table S1).

The microscopy results were consistent with the accompanying online measurements. Specifically, the proportion of organic matter measured by AMS was >90% in the Aitken range and >80% in the accumulation range, in which the proportion of sulfate increased (Fig. 2D). The submicrometer organic mass concentrations determined by means of AMS were higher than the corresponding SEM results, which is probably due to partial evaporation (14). The average oxygen-to-carbon ratio of 0.44 and the mass spectra observed during AMAZE-08 for the submicrometer organic matter are in good agreement with laboratory studies of biogenic SOA from isoprene and terpene oxidation (9, 15). PBA compounds detectable with AMS, such as proteins, amino acids, and carbohydrates, contributed less than 5% to the submicrometer particulate matter (9).

The predominance of SOA is further reflected in the effective hygroscopicity parameter κ determined through size-resolved CCN measurements (10). This parameter describes the influence of chemical composition on the ability of particles to absorb water vapor and form cloud droplets. Throughout the campaign, the κ values in the Aitken range were nearly constant at κ ≈ 0.1, which is in agreement with laboratory investigations of biogenic SOA from isoprene and terpene oxidation (4, 16) and much lower than the κ values of ammonium sulfate, sodium chloride, and other inorganic salts commonly observed in

aerosols (0.6 to 1.3) (17). In the accumulation mode size range (0.1 to 1 μm), κ increased to ~0.15 as the proportion of sulfate increased to ~10% (Fig. 2D). Nevertheless, the effective hygroscopicity remained lower by a factor of approximately two than the approximate global continental average value of κ ≈ 0.3 (10, 18).

The supermicrometer fraction with a local maximum (coarse mode) around 2 to 3 μm consisted mostly of PBA particles with a number fraction of ~80% (mass fraction 85%) plus some mineral dust and mixed SOA-inorganic particles with number fractions of 10 and 6%, respectively (Fig. 2, A and C, and tables S1 and S2). The SEM results were consistent with online measurements of fluorescent biological aerosol (FBA) particles, which can be regarded as a lower-limit proxy for PBA particles (19, 20). The number and mass fractions of supermicrometer FBA particles were 40 and 64%, respectively (Fig. 2, B and D, and tables S1 and S2).

Measurements and modeling of IN concentrations during AMAZE-08 suggest that ice formation in Amazon clouds at temperatures warmer than –25°C is dominated by PBA particles (20). Although the number concentration of such efficient biological IN is low (about 1 to 2 L^{-1}), they are nevertheless the first to initiate ice formation and can have a strong influence on the evolution of clouds and precipitation (21–23). At temperatures colder than –25°C, both locally emitted PBA and mineral dust particles imported from the Sahara desert can act as IN and induce cold rain formation. The IN activity of mineral dust may in fact also be influenced by biological materials, as suggested in earlier studies that include aircraft observations of ice cloud residuals (21, 24). In any case, PBA particles appear to be the most efficient IN and, outside of Saharan dust episodes, also the most abundant IN in the Amazon Basin. Moreover, the supermicrometer particles can also act as "giant" CCN, generating
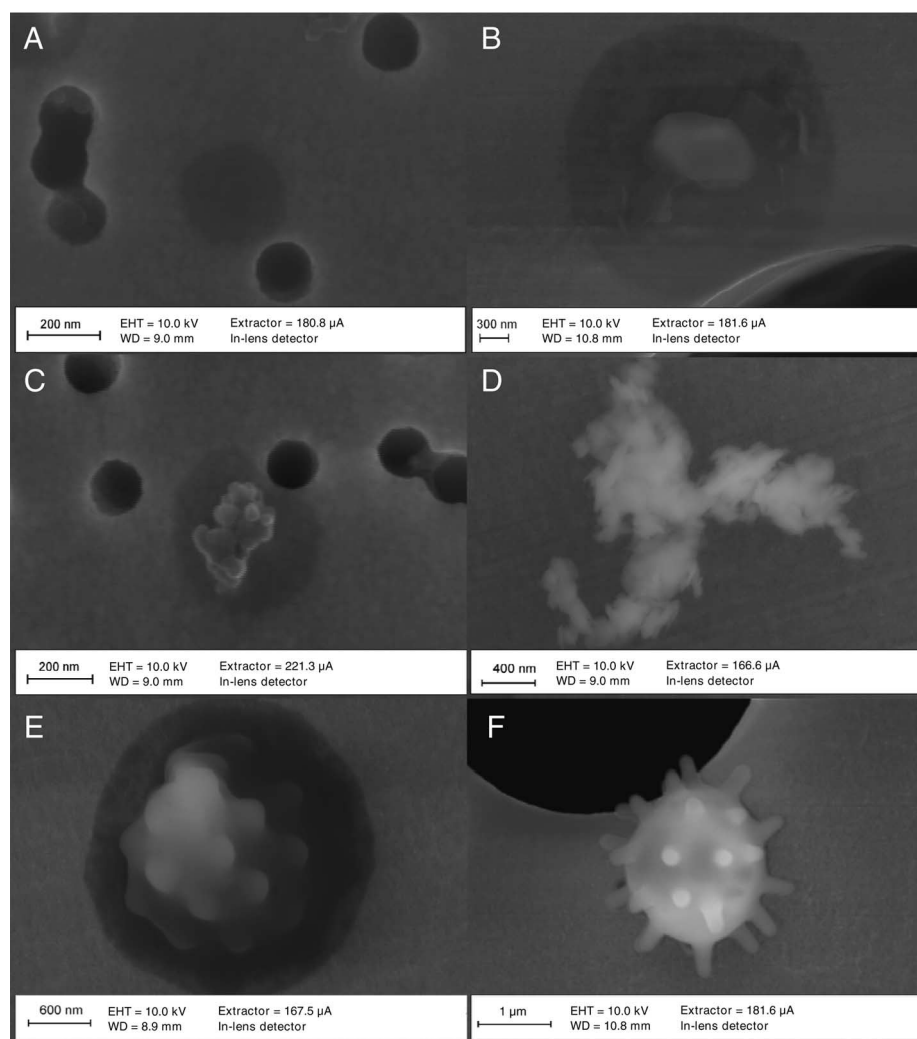

Fig. 1. Characteristic particle types observed by means of SEM of filter samples collected during AMAZE-08 (3 to 13 March 2008). (**A**) SOA droplet. (**B**) Mixed SOA-inorganic particle. (**C**) Pyrogenic carbon particle with organic coating. (**D**) Mineral dust particle without coating. (**E** and **F**) PBA particles (E) with and (F) without organic coating. SOA droplets and organic coatings appear dark gray, filter pores appear black, and filter material appears light gray (8).

large droplets and inducing warm rain without ice formation (2, 21).

The low aerosol concentrations and the high proportions of secondary organic and primary biological matter suggest that the climate system interactions between aerosols, clouds, and precipitation over pristine rainforest regions may substantially differ from both pristine marine regions ("green ocean" versus "blue ocean") as well as from polluted environments (2, 25). Model calculations using the aerosol size distributions and the hygroscopicity parameters determined in AMAZE-08 suggest that the activation of CCN in convective clouds over the pristine Amazonian rainforest is aerosol-limited, which means that

the number of cloud droplets is directly proportional to the number of aerosol particles (fig. S1) (26). In contrast, the formation of cloud droplets in polluted environments (including parts of the Amazon Basin influenced by intense biomass burning during the dry season), tends to be updraft-limited, which means that the number of cloud droplets depends primarily on the updraft velocity (26). In these environments, the abundance of CCN is usually dominated by anthropogenic particles from sources related to combustion processes (18).

Over the pristine Amazonian rainforest, convective clouds for which biogenic SOA particles serve as CCN may in turn promote the formation

of new SOA particles. During AMAZE-08, no new particle formation events were observed, which is consistent with earlier Amazonian aerosol studies (6, 7) but unlike most other continental regions of the world (27, 28). The low abundance of nucleation mode particles (<30 nm) (Fig. 2B, DMPS) and the relatively high abundance of SOA particles in the Aitken mode suggest, by inference, that new particle formation occurred in the free troposphere, possibly in the outflow of convective clouds, and that the newly formed particles were transported from aloft into the boundary layer, possibly in the downdraft of convective clouds (6, 7, 29, 30). Similarly, precipitation induced by PBA particles acting as IN or giant CCN sustains the reproduction of plants and microorganisms in the ecosystem from which both the SOA precursors and the PBA particles are emitted (such as bacteria, fungi, pollen, and plant debris) (6, 11). Accordingly, the Amazon Basin can be pictured as a biogeochemical reactor using the feedstock of plant and microbial emissions in combination with high water vapor, solar radiation, and photo-oxidant levels to produce SOA and PBA particles (31, 32). The biogenic aerosol particles serve as nuclei for clouds and precipitation, sustaining the hydrological cycle and biological reproduction in the ecosystem (Fig. 3). The feedback mechanisms involved may be important for stabilizing the Amazonian rainforest ecosystem and may also be generally relevant for the evolution of ecosystems and climate on global scales and in the Earth's history. To test this hypothesis, we suggest further studies and long-term observations of aerosol properties and aerosol-cloud-precipitation interactions under pristine conditions in other regions and climatic zones with high biological activity, including tropical, temperate, and boreal forests.

Fig. 2. Prevalence of different aerosol types in the (**A** and **B**) number size distribution (dN/dlog$D$) and (**C** and **D**) mass size distribution (dM/dlog$D$) plotted against particle diameter (D) as observed during AMAZE-08 (3 to 13 March 2008). Single particle analysis of filter samples was performed by means of SEM, and on-line measurements were made by means of differential mobility particle sizing (DMPS, <1 μm), aerosol mass spectrometry (AMS, < 1 μm), and ultraviolet aerodynamic particle sizing (UV-APS, >1 μm). Relative uncertainties are in the range of ~10 to 50% (8). There is a change of scales at D = 1 μm (left versus right ordinate).
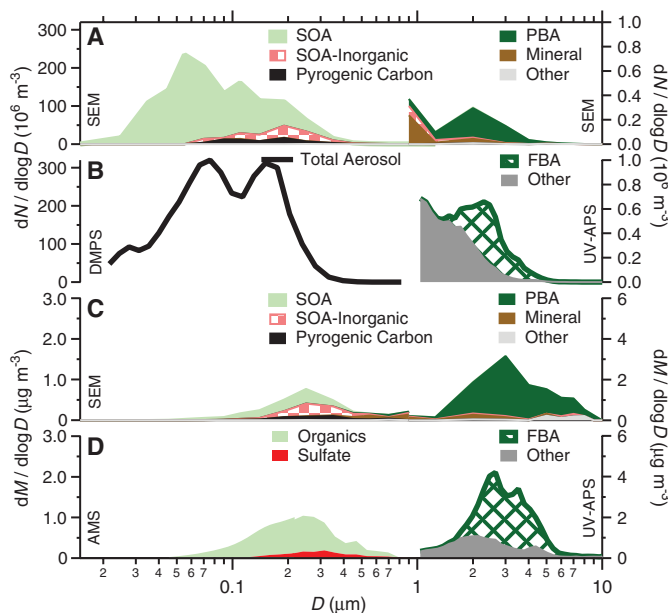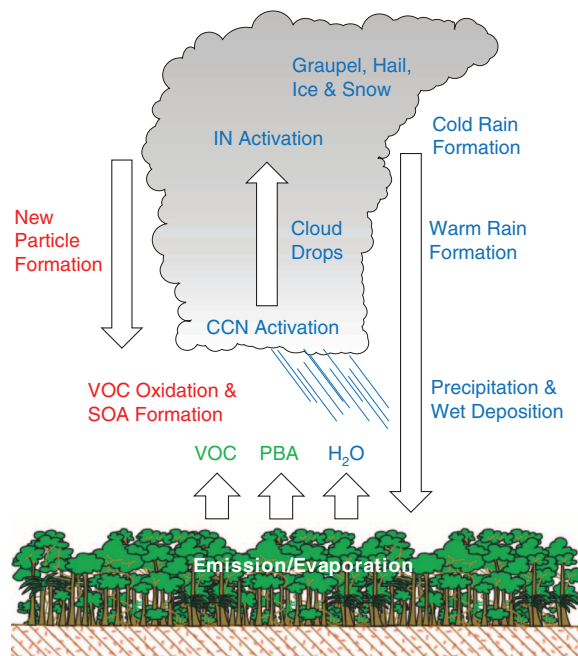

Fig. 3. Aerosol and water cycling over the pristine rainforest. SOA formed by photo-oxidation of volatile organic compounds (VOC) and PBA emitted from biota in the rainforest (plants and microorganisms) serve as biogenic nuclei for CCN and IN, which induce warm or cold rain formation, precipitation, and wet deposition of gases and particles.

References and Notes

1. S. Solomon et al., *IPCC 4th Assessment Report* (Cambridge Univ. Press, Cambridge, 2007).
2. D. Rosenfeld et al., *Science* **321**, 1309 (2008).
3. B. Stevens, G. Feingold, *Nature* **461**, 607 (2009).
4. J. L. Jimenez et al., *Science* **326**, 1525 (2009).
5. M. O. Andreae, *Science* **315**, 50 (2007).
6. S. T. Martin et al., *Rev. Geophys.* **48**, RG2002 (2010).
7. S. T. Martin et al., *Atmos. Chem. Phys. Discuss.* **10**, 18139 (2010).
8. Materials and methods are available as supporting material on *Science* Online.
9. Q. Chen et al., *Geophys. Res. Lett.* **36**, L20806 (2009).
10. S. S. Gunthe et al., *Atmos. Chem. Phys.* **9**, 7551 (2009).
11. W. Elbert, P. E. Taylor, M. O. Andreae, U. Pöschl, *Atmos. Chem. Phys.* **7**, 4569 (2007).
12. J. Fröhlich-Nowoisky, D. A. Pickersgill, V. R. Després, U. Pöschl, *Proc. Natl. Acad. Sci. U.S.A.* **106**, 12814 (2009).
13. I. Koren et al., *Environ. Res. Lett.* **1**, 014005 (2006).
14. K. S. Johnson et al., *Environ. Sci. Technol.* **42**, 6619 (2008).
15. M. Hallquist et al., *Atmos. Chem. Phys.* **9**, 5155 (2009).
16. S. M. King et al., *Atmos. Chem. Phys.* **10**, 3953 (2010).
17. M. D. Petters, S. M. Kreidenweis, *Atmos. Chem. Phys.* **7**, 1961 (2007).
18. M. O. Andreae, D. Rosenfeld, *Earth Sci. Rev.* **89**, 13 (2008).
19. J. A. Huffman, B. Treutlein, U. Pöschl, *Atmos. Chem. Phys.* **10**, 3215 (2010).
20. A. J. Prenni et al., *Nat. Geosci.* **2**, 402 (2009).

21. O. Möhler, P. J. DeMott, G. Vali, Z. Levin, *Biogeosciences* **4**, 1059 (2007).
22. B. C. Christner, C. E. Morris, C. M. Foreman, R. M. Cai, D. C. Sands, *Science* **319**, 1214 (2008).
23. R. M. Bowers *et al.*, *Appl. Environ. Microbiol.* **75**, 5121 (2009).
24. K. A. Pratt *et al.*, *Nat. Geosci.* **2**, 398 (2009).
25. M. O. Andreae *et al.*, *Science* **303**, 1337 (2004).
26. P. Reutter *et al.*, *Atmos. Chem. Phys.* **9**, 7067 (2009).
27. M. Kulmala *et al.*, *J. Aerosol Sci.* **35**, 143 (2004).
28. J. Merikanto, D. V. Spracklen, G. W. Mann, S. J. Pickering, K. S. Carslaw, *Atmos. Chem. Phys.* **9**, 8601 (2009).
29. R. Krejci *et al.*, *Atmos. Chem. Phys.* **5**, 1527 (2005).
30. A. M. L. Ekman *et al.*, *Geophys. Res. Lett.* **35**, L17810 (2008).
31. U. Kuhn *et al.*, *Atmos. Chem. Phys.* **7**, 2855 (2007).
32. J. Lelieveld *et al.*, *Nature* **452**, 737 (2008).
33. Support from a large number of colleagues, agencies, and institutions is gratefully acknowledged as detailed in the supporting online material.

Melting of Peridotite to 140 Gigapascals

G. Fiquet,[1]* A. L. Auzende,[1] J. Siebert,[1] A. Corgne,[2,3] H. Bureau,[1] H. Ozawa,[1,4] G. Garbarino[5]

Interrogating physical processes that occur within the lowermost mantle is a key to understanding Earth's evolution and present-day inner composition. Among such processes, partial melting has been proposed to explain mantle regions with ultralow seismic velocities near the core-mantle boundary, but experimental validation at the appropriate temperature and pressure regimes remains challenging. Using laser-heated diamond anvil cells, we constructed the solidus curve of a natural fertile peridotite between 36 and 140 gigapascals. Melting at core-mantle boundary pressures occurs at 4180 ± 150 kelvin, which is a value that matches estimated mantle geotherms. Molten regions may therefore exist at the base of the present-day mantle. Melting phase relations and element partitioning data also show that these liquids could host many incompatible elements at the base of the mantle.

Geophysical and geochemical observations favor the presence of chemical heterogeneities in the lowermost mantle. These are thought to be either primitive mantle residues (*1*), dense subducted slab components (*2*), products of chemical interactions between the core and mantle (*3*, *4*), or dense melts perhaps as old as the Earth itself (*5*). The core-mantle boundary is a complex region that has been the focus of numerous geophysical studies. Seismologic studies suggest the presence of two large low-shear velocity provinces (LLSVPs) under the African continent and in the pacific basin (*6*, *7*). The consensus view is that these slow regions (which are possibly up to 1000 km thick) exhibit an anomalously low shear velocity and increased bulk modulus but are not usually thought to be partially molten (*8*). Additionally, extensively documented ultralow-velocity zones (ULVZs) correspond to localized features at the core mantle boundary (CMB), with strong reductions in seismic velocities (in the range of 10 to 30%) for both P and S waves (*9*, *10*); the interpretation

is that these zones may be partially molten (*5*). Recent high-resolution waveform studies also find evidence that the ULVZ material is denser than the surrounding mantle (*11*). These partially molten regions have not been detected to be laterally continuous and have a thickness ranging from a few kilometers up to about 50 km.

It is attractive to link these observations with an episode of extensive melting that probably affected the primitive Earth, leading to the formation of a deep magma ocean. If the evolution of a terrestrial magma ocean resulted in the formation of a layer of melt at the base of the mantle early in Earth history, its survival depends on whether it was (and maybe still is) gravitationally and chemically stable (*12*). If this is the case, such a layer would be an ideal candidate for an unsampled geochemical reservoir hosting a variety of incompatible species, notably the planet's missing budget of heat-producing elements (*13*). The presence of high-pressure melts would also have consequences for chemical reactions between the mantle and core, the dynamics of the lowermost mantle, and the heat flow across the CMB.

To constrain the existence of melt at the base of the mantle, we performed melting experiments on a fertile peridotite composition over a range of lower-mantle pressures between 36 and 140 GPa using a laser-heated diamond-anvil cell (DAC) coupled with in situ synchrotron measurements (*14*). Our study thus extends the pressure range of previous measurements (*15*, *16*) of the solidus and liquidus temperatures of a mantle-like composition to depths exceeding those of the CMB at 2900 km. The starting material used for the high-

pressure high-temperature melting experiments is a natural KLB-1 peridotite (*14*). To ensure chemical homogeneity at the smallest scale and Fe as mostly Fe^{2+}, a glass was prepared by using an aerodynamic levitation device coupled with CO_2 laser heating under slightly reducing conditions of oxygen fugacity (*17*). At high temperature, pressures were measured from cell parameters of the magnesium perovskite $(Mg,Fe)SiO_3$ by using a thermal equation of state recently reported for the same KLB-1 peridotitic starting material as
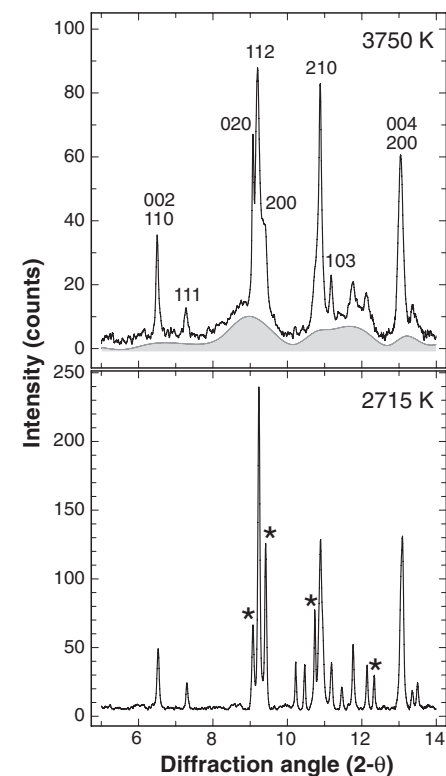

Fig. 1. Diffraction patterns collected at 61 GPa after normalized reference background subtraction: subsolidus at 2715 K (**bottom**) and above solidus at 3750 K (**top**). The diffuse scattering liquid contribution is outlined by the shaded area as a guide; it does not correspond to a physical structural model of the liquid. HKL indexes are given for remaining diffraction peaks that can be assigned to magnesium silicate perovskite, observed above the solidus temperature at this pressure (top). Stars denote diffraction peaks of Ca-perovskite and ferropericlase affected by partial melting at these conditions (bottom).

[1]Institut de Minéralogie et de Physique des Milieux Condensés, Institut de Physique du Globe de Paris, Université Pierre et Marie Curie, UMR CNRS 7590, Université Paris Diderot, 140 rue de Lourmel, 75015 Paris, France. [2]Institut de Physique du Globe de Paris, Equipe de Minéralogie à l'Institut de Minéralogie et de Physique des Milieux Condensés, 140 rue de Lourmel, 75015 Paris, France. [3]Observatoire Midi-Pyrénées, UMR CNRS 5562, 14 rue Edouard Belin, 31400 Toulouse, France. [4]Department of Earth and Planetary Sciences, Tokyo Institute of Technology 2-12-1 Ookayama, Meguro-ku, Tokyo 152-8551, Japan. [5]European Synchrotron Radiation Facility, BP220, 38043 Grenoble cedex, France.

*To whom correspondence should be addressed. E-mail: guillame.fiquet@impmc.upmc.fr

can then engage distinct protein modification pathways. While such a mechanism would be unusual, it is not completely unprecedented. Recent work on the eukaryotic signal recognition particle also points to the potential importance of nascent proteins folding within the ribosomal tunnel (*11*). Whatever the exact mechanism, the discovery of Zhang *et al*. that synonymous codon changes can so profoundly change the role of a protein adds a

new level of complexity to how we interpret the genetic code.

References and Notes
1. S. Seppälä, J. S. Slusky, P. Lloris-Garcerá, M. Rapp, G. von Heijne, *Science* **328**, 1698 (2010).
2. F. Zhang. S. Saha. S. Shabalina. A. Kashina, *Science* **329**, 1534 (2010).
3. A. Kaji, H. Kaji, G. D. Novelli, *Biochem. Biophys. Res. Commun.* **10**, 406 (1963).
4. C. C. Wong *et al*., *PLoS Biol.* **5**, e258 (2007).
5. R. Rai *et al*., *Development* **135**, 3881 (2008).
6. M. Karakozova *et al*., *Science* **313**, 192 (2006).
7. A. S. Kashina, *Trends Cell Biol.* **16**, 610 (2006).
8. T. Tuller *et al*., *Cell* **141**, 344 (2010).
9. G. Cannarozzi *et al*., *Cell* **141**, 355 (2010).
10. G. Kramer, D. Boehringer, N. Ban, B. Bukau, *Nat. Struct. Mol. Biol.* **16**, 589 (2009).
11. U. Berndt, S. Oellerer, Y. Zhang, A. E. Johnson, S. Rospert, *Proc. Natl. Acad. Sci. U.S.A.* **106**, 1398 (2009).
12. Supported by NIH (GM65183) and the Unity through Knowledge Fund of Croatia (10/07).

ATMOSPHERIC SCIENCE

Aerosols in Clearer Focus

Urs Baltensperger

Two studies provide insight into aerosol characteristics and cloud formation in regions with widely different aerosol concentrations.

Atmospheric aerosols—microscopic liquid or solid particles suspended in Earth's atmosphere—can harm human health (*1*) as well as influence climate by absorbing and reflecting solar radiation and modifying cloud formation (*2*). Our ability to fully describe the role of aerosols in the climate system, however, has been limited by uncertainty surrounding aerosol distribution and characteristics. Two papers in this issue help reduce this uncertainty by providing data from two regions where coverage was poor. On page 1488, Clarke and Kapustin (*3*) detail aerosol profiles from both relatively pristine and polluted areas over the Pacific Ocean. On page 1513, Pöschl *et al*. (*4*) report on aerosols and cloud formation over the Amazon, where conditions may approximate those that existed in preindustrial times.

Health-related monitoring typically focuses on measuring aerosol mass concentrations, but a suite of additional variables comes into play when dealing with climate issues. Climate researchers, for instance, want to know how aerosols scatter or absorb light to calculate aerosol optical depth (AOD), an important measure of atmospheric transparency, which can directly affect climate. They also want to know how many cloud condensation nuclei (CCN) are available to form cloud droplets; the radiative properties of clouds are influenced by the CCN concentration, an effect known as the indirect aerosol effect on climate (*5*). Clarke and Kapustin present data on AOD and a CCN proxy (the number
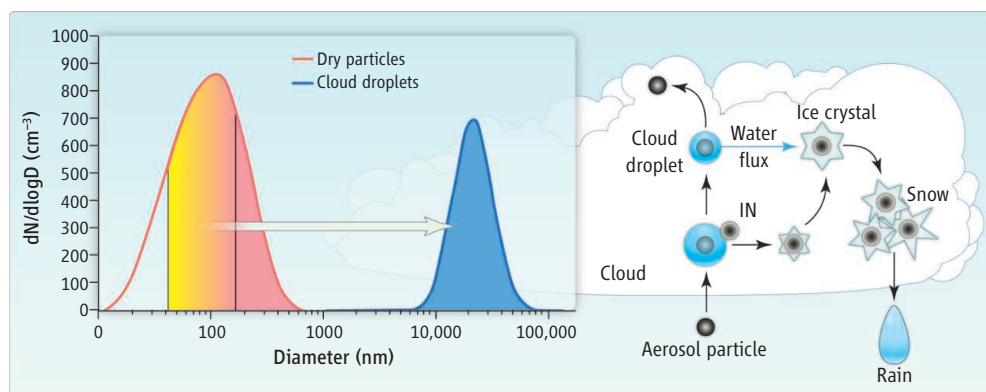
Aerosols into cloud droplets. (**Left**) The red curve presents a typical number size distribution of dry aerosol particles from the mountain site Jungfraujoch, Switzerland (*11*). The red shaded area represents particles that are activated to cloud droplets at a very low supersaturation (0.1%); orange and yellow areas represent activated particles for increasing supersaturation up to 1%. Critical diameters for Jungfraujoch aerosols can vary slightly with water solubility, surface tension, or mixing state (*12*); however, size is the most important parameter (*13*). The blue distribution represents an example of the size distribution of cloud droplets measured at the Jungfraujoch (*7*). (**Right**) When ice crystals are formed, water vapor is transported from the cloud droplets to the ice crystals because of the lower saturation vapor pressure over ice than over liquid water. This eventually results in evaporation of the cloud droplets, and the radiative properties of the cloud are no longer influenced by the number of CCN but only by the properties of the ice nuclei (IN) and ice crystals.

of particles surviving a 1- to 2-s exposure to 300°C) from about 1000 vertical profiles collected over 13 years. The data show that, in the Pacific regions most influenced by anthropogenic activities such as the burning of fossil fuels and biomass, AOD, CCN, and all other measured aerosol variables are higher—by more than an order of magnitude—than in cleaner regions. They conclude that increased aerosols from combustion are directly and indirectly influencing climate.

Andreae (*6*) argues that prehuman aerosol levels were very similar over continents and oceans. He concludes that, before the onset of human-induced pollution, the microphysical properties of clouds that formed over the continents resembled those that formed over the oceans. Today, however, cloud processes over most continents are shaped

by the effects of human perturbation.

Pöschl *et al*. report on cloud formation over one region where preindustrial conditions may still occur: the Amazon during the wet season. They characterized aerosols in air masses that moved over the region for an 11-day period in March 2008. They found that the majority of CCN were composed of secondary organic material formed by oxidation of gaseous biogenic precursors (apparently from forest biota). They showed that aerosol-cloud interactions in this environment are distinctly different from those in polluted regions. In particular, they suggest that cloud formation over the pristine Amazon is limited by the number of available aerosol particles; in contrast, in polluted regions the formation of cloud droplets is limited by the velocity of the updrafts that carry particles into the

Paul Scherrer Institute, 5232 Villigen PSI, Switzerland. E-mail: urs.baltensperger@psi.ch

higher atmosphere, where they "activate" into cloud droplets.

Pöschl et al. report that low aerosol concentrations resulted in cloud droplet number concentrations that were nearly independent of the updraft velocity of a convective cloud, and substantially higher supersaturation levels than found in polluted areas. This in turn meant that particles could activate to cloud droplets at a lower (smaller) critical diameter than in polluted areas. This modeling result is confirmed by measurements at the high-altitude (3580 m) station Jungfraujoch, Switzerland. There, the median of the activation diameter decreased from about 100 nm for particle concentrations (with diameter $D > 100$ nm) greater than 100 cm^{-3} to about 65 nm for particle concentrations below 100 cm^{-3} (7). The effect of varying supersaturation is illustrated in the figure: At high supersaturation, a much higher fraction of the aerosol particles is activated to cloud droplets than at low supersaturation.

Pöschl et al. also report on ice nuclei (IN),

particles that initiate ice formation at a temperature considerably above the freezing temperature of water (roughly –40°C). Supermicron-sized particles over the Amazon consisted mostly of primary biological aerosol particles that showed substantial IN activity. Precipitation occurs when these supermicron particles act as "giant" CCN (in warm rain) or IN (when ice formation is involved). The impact of aerosol particles on precipitation is different for warm and cold clouds. In warm clouds, increased CCN concentrations slow the conversion of cloud droplets into raindrops by nucleating larger concentrations of smaller drops, which are slower to coalesce into raindrops (8). In cold clouds, the situation is much more complex. The saturation vapor pressure is lower over ice than over liquid water; this transports water vapor from the cloud droplets to the ice crystals as soon as ice crystals form in liquid clouds (the so-called Wegener-Bergeron-Findeisen process) (9). This results in evaporation of the cloud droplets and a very low fraction of activated

CCN (10). In these clouds, the radiative properties of the cloud are no longer influenced by the number of CCN but only by the properties of the IN and ice crystals. These processes are important for both the hydrological cycle and the radiative properties of clouds and clearly call for more research.

References
1. C. A. Pope, D. W. Dockery, *J. Air Waste Manage. Assoc.* **56**, 709 (2006).
2. IPCC, *Contribution of Working Group I to the Fourth Assessment Report of the Intergovernmental Panel on Climate Change*, S. Solomon et al., Eds. (Cambridge Univ. Press, Cambridge, UK), www.ipcc.ch/ipccreports/ar4-wg1.htm (2007).
3. A. Clarke, V. Kapustin, *Science* **329**, 1488 (2010).
4. U. Pöschl et al., *Science* **329**, 1513 (2010).
5. S. Twomey, *J. Atmos. Sci.* **34**, 1149 (1977).
6. M. O. Andreae, *Science* **315**, 50 (2007).
7. S. Henning et al., *Tellus* **54B**, 82 (2002).
8. D. Rosenfeld et al., *Science* **321**, 1309 (2008).
9. W. Findeisen, *Meteorol. Z.* **55**, 121 (1938).
10. B. Verheggen et al., *J. Geophys. Res.* **112**, D23202 (2007).
11. E. Weingartner, S. Nyeki, U. Baltensperger, *J. Geophys. Res.* **104**, 26809 (1999).
12. G. McFiggans et al., *Atmos. Chem. Phys.* **6**, 2593 (2006).
13. U. Dusek et al., *Science* **312**, 1375 (2006).

BIOCHEMISTRY

A Never-Ending Story

Revealing another way cells make DNA building blocks, this time with manganese.

Britt-Marie Sjöberg

More than 50 years ago, Reichard and colleagues elucidated how cells make their DNA building blocks—the deoxyribonucleotides or dNTPs (1). They found that the enzyme ribonucleotide reductase (RNR) converts ribonucleotides (RNA building blocks) to corresponding dNTPs. One would expect that such a central pathway for all living cells would be meticulously mapped by now. Yes—and no. Researchers have described several classes and subclasses of RNRs (see the figure) that appear to have the same evolutionary origin (2–5), but involve different chemical cofactors, and so enable cells to construct dNTPs under different environmental conditions. Whenever the field seems settled, however, fascinating new aspects appear (1, 2). On page 1526 of this issue, Boal et al. (3) report crystal structures of RNR complexes from the bacterium *Escherichia coli* that, together with earlier studies, confirm and neatly illuminate yet another way cells can construct dNTPs, this time with the help of manganese (Mn).

Early researchers initially identified two classes of RNR: class I, which is characterized by a nonheme diiron center and a protein-derived tyrosyl radical (Fe^{III}_2-Tyr•); and class II, which involve the vitamin B_{12} coenzyme 5′-deoxyadenosylcobalamin (AdoCbl). Both of these RNR classes operate when oxygen is present (aerobic conditions). Later, investigators identified an anaerobic class III RNR, which involves a glycyl radical cofactor (Gly•) generated by an iron-sulfur cluster that cleaves S-adenosylmethionine (AdoMet). Despite structural differences and the involvement of different cofactors (see the figure), all RNR classes have a common origin and generate a transient thiyl radical (Cys•) in the active site.

In 1988, investigators isolated a Mn–dependent RNR from *Corynebacterium ammoniagenes* (6). It was not recognized as its own class, however; gene sequencing classified it as part of RNR class Ib, a subclass of class I. In addition, the role of Mn was unclear, since the new RNR was active in vitro with an iron cofactor (Fe^{III}_2-Tyr•) (7). Now, Boal et al., together with Cox et al. (8), highlight the importance of the Mn form of the class Ib RNR in *C. ammoniagenes* and

E. coli. The work also highlights the role of the protein NrdI, a flavodoxin that is a crucial player in the formation of Mn-RNR. NrdI is encoded in the same operon as NrdE and NrdF, the two components of the known class Ib RNR. NrdI is essential for the formation of Tyr• in Mn-NrdF (9).

The NrdIs are unusual flavodoxins. They are smaller than classical flavodoxins, with one notable variation in the loop that interacts with the flavin mononucleotide (FMN) (3, 10). Recent structures for NrdIs from *Bacillus anthracis* (10), *Bacillus cereus* (11), and *E. coli* (3) cover the three redox forms of FMN (oxidized, semiquinone, and hydroquinone). Whereas the two redox potentials of classical flavodoxin differ by more than 100 mV (12), *E. coli* NrdI maintains two almost identical redox potentials (9). The semiquinone form is thus transient in *E. coli* NrdI, which probably functions as a two-electron donor. Several NrdIs differ markedly from classical flavodoxin in their isoelectric points (pIs). Whereas flavodoxins have very similar pIs (4.5 ± 0.6), those of *E. coli* and *C. ammoniagenes* NrdIs are much higher, and *B. cereus* and *B. anthracis* NrdIs have pIs like those of flavodoxins (11). Both *B. cereus* and *B. anthracis* NrdIs

Department of Molecular Biology and Functional Genomics, Stockholm University, SE-10691 Stockholm, Sweden E-mail: britt-marie.sjoberg@molbio.su.se

Supporting Online Material for

Rainforest Aerosols as Biogenic Nuclei of Clouds and Precipitation in the Amazon

U. Pöschl,* S. T. Martin,* B. Sinha, Q. Chen, S. S. Gunthe, J. A. Huffman, S. Borrmann,
D. K. Farmer, R. M. Garland, G. Helas, J. L. Jimenez, S. M. King, A. Manzi,
E. Mikhailov, T. Pauliquevis, M. D. Petters, A. J. Prenni, P. Roldin, D. Rose,
J. Schneider, H. Su, S. R. Zorn, P. Artaxo, M. O. Andreae

*To whom correspondence should be addressed. Email: u.poschl@mpic.de (U.P.);
scot_martin@harvard.edu (S.T.M.)

This PDF file includes:

Materials and Methods

SOM Text

Fig. S1

Tables S1 to S6

References and Notes

Supporting Online Material for

Rainforest aerosols as biogenic nuclei of clouds and precipitation

in the Amazon

U. Pöschl[*], S. T. Martin[*], B. Sinha, Q. Chen, S. S. Gunthe, J. A. Huffman, S. Borrmann,
D. K. Farmer, R. M. Garland, G. Helas, J. L. Jimenez, S. M. King, A. Manzi,
E. Mikhailov, T. Pauliquevis, M. D. Petters, A. J. Prenni, P. Roldin, D. Rose,
J. Schneider, H. Su, S. R. Zorn, P. Artaxo, M. O. Andreae

*To whom correspondence should be addressed. Email: u.poschl@mpic.de (U.P.);
scot_martin@harvard.edu (S.T.M.)

This file includes:

Materials and Methods

Supporting Text

Supporting References and Notes

Fig. S1

Tables S1, S2, S3, S4, S5, S6

S1   Materials and Methods

S1.1   Measurement location and aerosol sampling

The Amazonian Aerosol Characterization Experiment (AMAZE-08) was carried out during the wet season over the period of 7 February to 14 March 2008 at a remote site in pristine terra firme rainforest 60 km NNW of the city of Manaus in Brazil (2.59454° S, 60.20929° W, 90 m above sea level). The observational tower (TT34) was located in the Reserva Biologica do Cuieiras and managed by the Instituto Nacional de Pesquisas da Amazonia (INPA) and the Large-Scale Biosphere-Atmosphere Experiment in Amazonia (LBA). The sampled air masses came mainly from the northeast across some 1600 km of almost untouched forest, allowing the study of pristine tropical rainforest conditions. Ten-day back trajectories indicated arrival of air masses from the northeast, originating over the Atlantic Ocean in the direction of Cape Verde and the Canary Islands (*1*). This study focuses on measurement results obtained during the period of 3-13 March 2008, which exhibited particularly little influence of long range transport or regional air pollution (*1-3*). The average temperature, pressure and relative humidity measured at the top of the observational tower TT34 during the period of 3-13 March were (297±2) K, (993±5) hPa, and (93±10) % RH (arithmetic mean ± standard deviation). Aerosols were sampled from the top of the observational tower (39 m above the ground, ~5 m above the forest canopy) and collected or analyzed in a measurement container at the bottom of the tower. Concentration data were normalized to standard temperature and pressure (273 K, 1000 hPa). Most instruments were connected to a laminar flow inlet with a pre-impactor removing particles with aerodynamic diameters larger than ~7 μm. One of the aerosol mass spectrometers used in this study was connected to a turbulent flow inlet without pre-impactor (*2*), but the results are fully consistent with the instrument connected to the laminar flow inlet (*1*). For details about the meteorological conditions, sampling devices and measurement instruments see Martin et al. (*1*) and related publications (*2–4*).

S1.2   Collection of filter samples

Aerosol samples for microscopic analysis were collected with a stacked filter unit using gold coated Nuclepore® polycarbonate filters with pore sizes of 5 μm for coarse particles and 0.2 μm for fine particles, respectively (*5*). The volumetric flow through the stacked filter unit was nominally 1 L min⁻¹. For the calculation of particle number and mass concentrations, the air sample volume was normalized to standard conditions (273 K, 1000 hPa). Due to flow control difficulties, the actual flow rates and sample volumes may have been smaller than the nominal value (deviations up to ~30%), which explains why the

2

absolute concentration values determined by scanning electron microscopy (SEM) were systematically lower than the concentrations determined by parallel online measurements. Note, however, that this uncertainty does not affect the SEM results on the mixing state and relative proportions of different types of particles. The three pairs of filter samples that were most representative for pristine rainforest conditions with minimal influence of air pollution and long range transport were collected during the following periods (UTC): 3 March 21:17 – 5 March 14:05 (40.9 h, Sample M4); 8 March 20:15 – 9 March 19:53 (23.6 h, Sample M8); 12 March 17:12 – 13 March 18:30 (25.3 h, Sample M12). The samples were analyzed by microscopy as specified below.

S1.3   SEM analysis

Scanning electron microscopy (SEM) images of aerosol particles were acquired using the secondary electron in-lens detector of a high-performance field emission instrument (LEO 1530 FESEM, EHT 10 keV, WD 9 mm). The in-lens detector enabled detection of thin organic particles and coatings which are usually not detectable with other detectors. The elemental composition of inorganic components was characterized using the Oxford Instruments ultra-thin-window energy-dispersive X-ray (EDX) detector, and the organic nature of SOA droplets and mixed SOA-inorganic particles was confirmed by NanoSIMS analysis as detailed below.

The filter samples were scanned using a semi-automated spot counting technique (*5, 6*) at a magnification of 6500 × (pixel size 88.9 nm) for coarse and 19500 × (pixel size 29.6 nm) for fine particle filters. Particles located on the predefined equidistant spots of the counting grid were automatically counted, and the recorded data were used to classify the particles according to size, composition, and mixing state. With spot counting, the probability for particles of a certain size and type to be counted is directly proportional to the 2-D surface area of the particles and the fraction of the filter surface covered by such particles. This relationship is used to upscale the counting results from the investigated filter area to the total filter area. More than 6400 points (>0.6% of the total filter area) on coarse particle filters and more than 2500 points (>0.07% of the total filter area) on fine particle filters were investigated, leading to an average particle count of 100 coarse and 275 fine mode particles per air sample (filter pair). The 2-D surface area of a particle was measured by counting the number of pixels the particle occupied in the secondary electron image and used to calculate the 2-D equivalent diameter (diameter of a circle with the same surface area). For particles coated with organic material, the 2-D surface area and equivalent diameters were determined

for the particle with and without coating. For fine particles this was done with separately acquired high resolution images (pixel size 0.6 nm to 15 nm).

In order to calculate the 3-D equivalent diameter (diameter of a spherical particle with the same volume), the shape and height of the deposited particles needs to be known or estimated in addition to the 2D equivalent diameter. The shape and height of deposited SOA droplets were measured by atomic force microscopy (AFM) as detailed below. The shape was approximately that of a spherical segment, and the height was on average 1/4 of the diameter of the circular footprint, corresponding to a contact angle of 52.5° between the filter and the droplet. This contact angle and spherical geometry were also assumed in the calculation of the volume of organic material in mixed SOA-inorganic particles and the volume of organic coatings. For solid particles with diameters <100 nm (pyrogenic carbon) as well as larger solid particles with near-circular footprints (PBA), the 3-D equivalent diameter was assumed to equal the 2-D equivalent diameter. For non-spherical solid particles >100 nm the volume and 3-D equivalent diameter were calculated assuming an average height of 2/3 of the 2-D equivalent diameter, to account for the fact that solid particles usually land and rest on their flat side when deposited on a filter. The scaling factor of 2/3 was obtained by analyzing the height of a subset of characteristic particles (SEM working distance at high resolution). The 3-D equivalent diameters were used for size distribution plots and further analyses. Particle masses were calculated assuming an approximate average density of 1.5 g cm^{-3} for all particle types. The SEM concentration data reported in the figures and tables of this manuscript were averaged over the three pairs of filter samples specified above. The estimated relative uncertainties are <10% for the relative proportions of different particle types and <50% for absolute particle number and mass concentrations.

S1.4 AFM analysis

The shape and height of SOA droplets deposited on the filters were determined by atomic force microscopy (AFM, C/P-Research, ThermoMicroscopes/Veeco Instruments, USA). The AFM instrument was operated in non-contact mode using reflective tapping mode etched silicon probes (RTESPA, Model MPP 11120) at frequencies close to 400 kHz (7). Lateral and vertical drifts were <5%.

S1.5 NanoSIMS analysis

The composition and mixing state of SOA droplets and mixed SOA-inorganic particles were investigated with a Cameca NanoSIMS 50 ion microprobe in multi-collection detector mode (simultaneously collecting C$^-$, O$^-$, CN$^-$, S$^-$ and Cl$^-$) by sputtering the sample with a 1 pA Cs$^+$ primary ion beam focused into a spot of 100 nm diameter. NanoSIMS

analysis was performed on filter sections previously analyzed by SEM to allow direct comparison of SEM particle classification with NanoSIMS results and identify the inorganic fraction of mixed droplets. First results of ongoing investigations confirm the organic nature of the SOA droplets, exhibiting signals of carbon, oxygen and nitrogen while sulfur and chlorine were not detectable. Note, however, that the available data do not exclude participation of sulfuric acid in new particle formation, because the minute amounts of sulfuric acid that might suffice for nucleation (a few tens of molecules per particle) would not be distinguishable from the filter background signal which determined the effective limit of detection (equivalent to particle mass fractions <1%) (*5*, *8*).

S1.6   UV-APS measurements

An ultraviolet aerodynamic particle sizer (UV-APS; TSI Inc. Model 3314) was used for online measurements of fluorescent biological aerosol (FBA) particles, which can be regarded as a lower-limit proxy for primary biological aerosol (PBA) particles (*4*, *9*). Instrumental details and data processing techniques have been described elsewhere (*4, 10, 11*). In short, the instrument performs aerodynamic particle sizing in the diameter range of 0.5 – 20.0 μm by measuring the time-of-flight between two He-Ne lasers. At diameters below 1 μm, the particle counting efficiency of the UV-APS drops below unity, and the potential for interference of fluorescence signals from non-biological particles increases (*4*). Thus, UV-APS data for particle diameters <1 μm were not used in this study. The instrument was operated in standard flow mode with a total volumetric flow rate of 5 L min^{-1}, and measurements were initiated every 5 minutes and integrated over a period of 299 s. Here we report average values for the period during which the three pairs of filter samples for SEM analysis were collected as specified above. Out of the 114 hours of filter collection time, 107 hours (94%) were covered by UV-APS measurements (1284 size distributions). Particle mass concentrations were calculated assuming an average density of 1.5 g cm^{-3} for all particle types. The estimated relative uncertainties of the UV-APS measurement data are <30%.

S1.7   DMPS and CCN measurements

Online measurements of aerosol particle size distributions and efficiency spectra of cloud condensation nuclei (CCN) were performed with a differential mobility particle sizer (DMPS: DMA, TSI 3071, sheath flow 10 L min^{-1}, CPC, TSI 3762, sample flow 1.0 L min^{-1}) coupled to a CCN counter (DMT-CCNC, Model 2, Droplet Measurement Technologies, total flow 0.5 L min^{-1}). Instrumental details and data processing techniques have been described elsewhere (*3, 12*). In short, the instrumental setup enables the measurement of aerosol particle size distributions (particle number vs. mobility equivalent diameter) and of CCN efficiency

spectra or activation curves (activated fraction vs. mobility equivalent diameter), from which effective hygroscopicity parameters (κ values) can be derived to characterize the influence of aerosol chemical composition on CCN activity. Due to instrument calibration and maintenance, less than 50% of the filter collection time for SEM analysis were directly covered by DMPS and CCN measurements. Thus, we use the average DMPS and CCN measurement results for the pristine focus period as defined by Gunthe et al. (*3*), which extends over the period of 6-12 March 2008. The estimated relative uncertainties of the DMPS and CCN measurement data are <20% (*3*).

S1.8   IN Measurements

Ice nuclei (IN) were measured using a continuous flow diffusion chamber (CFDC), which enables observation of freezing at controlled temperatures and humidities (*9*). An inertial impactor immediately downstream of the CFDC captured the ice particles formed in the chamber on transmission electron microscopy (TEM) grids. The residual nuclei were investigated by TEM with energy-dispersive X-ray spectroscopy (TEM-EDX) (*13*). The TEM results for ice nuclei were consistent with the SEM data for the total aerosol, with biogenic particles dominating the ice nuclei population during the period investigated in this study (collection time of filter samples for SEM analysis).

S1.9   AMS measurements

Online measurements of size-resolved chemical composition of non-refractory submicron aerosol particles were performed with two high-resolution time-of-flight aerosol mass spectrometers (HR-ToF-AMS, Aerodyne Research, referred as AMS for brevity) (*2*). Here we use the data acquired with both instruments during the collection time of filter samples for SEM analysis. For comparability with the DMPS and CCN data, the vacuum aerodynamic diameters measured with the AMS were converted into approximate mobility equivalent diameters as described by Gunthe et al. (*3*). The two AMS instruments were equipped with different aerodynamic inlets: one had better transmission for small particles (Harvard instrument: standard lens system) (*14*), the other was optimized for large particles (MPIC instrument: high pressure lens system - version 2, Aerodyne Research). Thus, we merged the two data sets to obtain maximum particle transmission and present a composite consisting of data from the Harvard instrument at $D \leq 215$ nm and from the MPIC instrument at $D > 215$ nm (Fig. 2). The relative deviations between the two instruments were <10% in the overlap region where both inlet systems achieve high particle transmission (~100%, 150–350 nm). The estimated overall uncertainties of the presented AMS data are <30%.

S2   Supporting Text

S2.1   Sources, transport and coating of particles

Due to coagulation and sedimentation, respectively, the atmospheric residence times of Aitken mode and coarse mode particles are generally shorter than those of accumulation mode particles, and the latter are more likely to undergo long-range transport (*15*). Therefore, Aitken and coarse mode are usually dominated by regional sources, whereas the accumulation mode is likely to contain particles from distant sources. Information about the mixing state and coating of particles can be used to gain further insight into atmospheric transport and aging processes.

Most mineral dust particles did not exhibit an organic coating (90-95% uncoated, Tabs. S1 and S2). Apparently these particles had undergone long-range transport from African deserts and spent little time in the lower troposphere over the rainforest where rapid coating would be expected due to intense photochemical activity and production of secondary organic aerosol (SOA) (*1, 2, 16-19*).

In contrast, inorganic salt particles containing sulfates and/or chlorides were practically always coated or mixed with organic material (SOA-inorganic particles, >99% coated, Tabs. S1 and S2), with the organic fraction being mostly larger than the inorganic fraction. Apparently these particles originated from regional or marine sources and were advected through the lower troposphere, where they formed together with SOA (secondary sulfates) (*1*) or were coated with SOA (potassium and sodium chloride from primary biological emissions or sea spray, respectively) (*1, 20*). In the submicron range ~70% of the mixed SOA-inorganic particles contained sulfate but no chloride, ~15% contained sulfate and chloride, and ~15% contained chloride but no sulfate. In the supermicron range practically all mixed SOA-inorganic contained both sulfate and chloride.

The balance between coated and uncoated PBA particles (~40-70% coated; Tables S1, S2) can be explained by the relatively short atmospheric residence time of these mostly coarse supermicron particles, which are preferentially emitted at night, when the photochemical production of SOA is low, and which undergo rapid dry or wet deposition (sedimentation or activation and precipitation as giant CCN or IN) (*4, 20–22*).

In contrast to PBA particles, pyrogenic carbon particles were present mostly in the submicron size range. Nevertheless, they exhibited a similar balance between coated and uncoated particles (~50-70% coated; Tables S1, S2). Similar to uncoated mineral dust, the uncoated pyrogenic carbon particles had most likely undergone long-range transport from African biomass burning sources and spent little time in the lower troposphere over the

rainforest (*1*). The coated pyrogenic carbon particles may have originated from regional sources and acquired an SOA coating during advection over the rainforest as outlined above for salt particles. Alternatively, their coating could also originate from their source in Africa or in the Amazon Basin (primary or secondary organic matter from biomass burning) (*1*).

In principle, the coating of mineral dust, PBA, and pyrogenic carbon particles could also be influenced by their surface properties, i.e., by different nucleation barriers for the condensation of an organic phase. In practice, however, it seems unlikely that SOA material with a vapor pressure sufficiently low to condense in pure SOA particles in the nucleation and Aitken mode size range (formation and growth of pure SOA droplets) would not condense on the surface of solid particles in the accumulation and supermicron size range. Laboratory studies with a surrogate compound for SOA found no preferential condensation on different types of substrates (*23*).

S2.2 *CCN activation and cloud droplet formation*

According to model calculations, the activation of cloud condensation nuclei (CCN) in convective clouds can proceed in three distinctly different regimes depending on the ratio between updraft velocity, w, and aerosol particle number concentration, N (*24*):

1) An aerosol-limited regime that is characterized by high w/N ratios, high maximum values of water vapor supersaturation (S_{max}), and high activated fractions of aerosol particles (N_{CD}/N; N_{CD} is the number concentration of cloud droplets). In this regime N_{CD} is almost directly proportional to N and nearly independent of w.

2) An updraft-limited regime that is characterized by low values of w/N, S_{max} and N_{CD}/N. In this regime N_{CD} is almost directly proportional to w and nearly independent of N.

3) An aerosol- and updraft-sensitive regime (transitional regime), which is characterized by intermediate parameter values and where N_{CD} depends non-linearly on both N and w.

In polluted regions with high aerosol concentrations, the activation of CCN typically occurs in the updraft-limited or transitional regime (*24*). Under these conditions the number of cloud droplets depends strongly on the updraft velocity at the cloud base. This is also the case when parts of the Amazon Basin are strongly influenced by biomass burning during the dry season (*25*).

To explore the regime of CCN activation and cloud droplet formation in pristine Amazonian rainforest air, we have performed numerical simulations using a cloud parcel model with detailed spectral microphysics (*24*) and the average hygroscopicity parameter and aerosol size distribution determined in AMAZE-08 (pristine focus period) (*3*): $\kappa = 0.14$, two

log-normal modes ($N = N_1 + N_2$) with a relative number concentration ratio of $N_1/N_2 = 0.81$, and with geometric mean diameter and standard deviation values of $D_{g,1} = 67$ nm and $\sigma_{g,1} = 1.32$ (Aitken mode) and $D_{g,2} = 150$ nm and $\sigma_{g,2} = 1.43$ (accumulation mode). In a series of 650 model runs the updraft velocity and the initial number concentration of aerosol particles have been varied systematically over the range of $w = 0.5\text{-}10$ m s^{-1} and $N = 10\text{-}1000$ cm^{-3} (model description and initialization as detailed by Reutter et al. (*24*)).

The model results are displayed in Figure S1. Panel A shows the number concentration of cloud droplets, N_{CD} (cm^{-3}) that are formed at the cloud base as a function of w and N. The corresponding activated fractions of aerosol particles (N_{CD}/N, %) and the maximum water vapor supersaturations reached in the ascending air masses (S_{max}, %) are shown in panels B and C, respectively. The dashed red line indicates the border between the aerosol-limited and transitional regimes, which is defined by a relative sensitivity ratio of $(\partial \ln N_{CD}/\partial \ln w)/(\partial \ln N_{CD}/\partial \ln N) = 1:4$. Above this line the near-perpendicular N_{CD} isopleths in panel A indicate that the cloud droplet number concentration is almost directly proportional to the aerosol number concentration and nearly independent of updraft velocity. The borderline of the aerosol-limited regime coincides with isopleths of $N_{CD}/N= 0.9$ and with S$_{max}$ = 0.8 % in panels B and C.

At the average aerosol concentration level observed during AMAZE-08 ($N \approx 200$ cm^{-3}), updraft velocities as low as 2 m s^{-1} are sufficient to induce water vapor supersaturations as high as 0.8% and to activate nearly all available aerosol particles. The updraft velocities at the base of precipitating cumulus and cumulonimbus clouds are typically higher than 2 m s^{-1} (*26–30*). The dotted blue box in Fig. S1 indicates a range of updraft velocities and aerosol concentrations that can be regarded as characteristic for the base of convective clouds over the Amazon. Most of this range is in the aerosol-limited regime. Thus, the initial number of cloud droplets formed in convective clouds over the pristine Amazonian rainforest is directly proportional to the number of aerosol particles and hardly influenced by the updraft velocity. Compared to the observed variability of particle number and size, the observed variability of particle hygroscopicity appears to play a relatively minor role (*3, 12, 24*).

The model results are consistent with observations of deep convective clouds formed under clean conditions over the "Green Ocean" of the Amazon Basin (*25, 31*). If the aerosol concentration is increased to the level of polluted continental regions ($>10^3$ cm^{-3}), the CCN activation process moves into the aerosol- and updraft-sensitive regime, the updraft velocity becomes important, and the number of cloud droplets increases, which can lead to changes in cloud evolution and precipitation (*25, 32*).

Supporting References and Notes

1. S. T. Martin, et. al., *Atmos. Chem. Phys.,* to be submitted (2010).

2. Q. Chen *et al.*, *Geophys. Res. Lett.* **36** (2009).

3. S. S. Gunthe *et al.*, *Atmos. Chem. Phys.* **9**, 7551 (2009).

4. J. A. Huffman, B. Treutlein, U. Pöschl, *Atmos. Chem. Phys.* **10**, 3215 (2010).

5. B. W. Sinha, P. Hoppe, J. Huth, S. Foley, M. O. Andreae, *Atmos. Chem. Phys.* **8**, 7217 (2008).

6. S. Amelinckx, D. Van Dycke, J. Van Landuyt, G. Van Tendeloo, *Handbook of Microscopy: Applications in Material Science, Solid-State Physics and Chemistry* (Wiley–VCH, Weinheim, 1998).

7. G. Helas, M. O. Andreae, *Atmos. Meas. Tech.* **1**, 1 (2008).

8. E. G. M. Werner *et al.*, *ChemBioChem*, **11,** (2010).

9. A. J. Prenni *et al.*, *Nature Geosci.* **2**, 401 (2009).

10. P. P. Hairston, J. Ho, F. R. Quant, *J. Aerosol Sci.* **28**, 471 (1997).

11. L. M. Brosseau *et al.*, *Aerosol Sci. Technol.* **32**, 545 (2000).

12. D. Rose *et al.*, *Atmos. Chem. Phys.* **10**, 3365 (2010).

13. M. S. Richardson *et al.*, *J. Geophys. Res. -Atmos.* **112** (2007).

14. P. S. K. Liu *et al.*, *Aerosol Sci. Technol.* **41**, 721 (2007).

15. C. Textor *et al.*, *Atmos. Chem. Phys.* **6**, 1777 (2006).

16. U. Kuhn *et al.*, *Atmos. Chem. Phys.* **7**, 2855 (2007).

17. M. Hallquist *et al.*, *Atmos. Chem. Phys.* **9**, 5155 (2009).

18. J. L. Jimenez *et al.*, *Science* **326**, 1525 (2009).

19. S. T. Martin *et al.*, *Rev. Geophys.* **48**, RG2002, doi:10.1029/2008RG000280 (2010).

20. W. Elbert, P. E. Taylor, M. O. Andreae, U. Pöschl, *Atmos. Chem. Phys.***7**, 4569 (2007).

21. O. Möhler, P. J. DeMott, G. Vali, Z. Levin, *Biogeosciences* **4**, 1059 (2007).

22. J. Fröhlich-Nowoisky, D. A. Pickersgill, V. R. Despres, U. Pöschl, *Proc. Nat. Acad. Sci.* **106**, 12814 (2009).

23. C.N. Cruz, S. N. Pandis, *Aerosol Sci. Technol.*, **31**, 392 (1999).

24. P. Reutter *et al.*, *Atmos. Chem. Phys.* **9**, 7067 (2009).

25. M. O. Andreae *et al.*, *Science* **303**, 1337 (2004).

26. A. H. Auer Jr, W. Sand. *J. Appl. Meteorol.* **5**, 461-466 (1966)

27. R. P. Davies-Jones, J. H. Henderson, *Pure Appl. Geophys.* **113**, 787 (1975).

28. P. Kollias, B. A. Albrecht, R. Lhermitte, A. Savtchenko, *J. Atmos. Sci.* **58**, 1750 (2001).

29. N. F. Anderson, C. A. Grainger, J. L. Stith, *J. Appl. Meteorol.* **44**, 731 (2005).

30. F. J. Nober, H. F. Graf, *Atmos. Chem. Phys.* **5**, 2749 (2005).

31. E. Freud, D. Rosenfeld, M. O. Andreae, A. A. Costa, P. Artaxo, *Atmos. Chem. Phys.* **8**, 1661 (2008).

32. D. Rosenfeld *et al.*, *Science* **321**, 1309 (2008).

Fig. S1. Droplet formation at the base of convective clouds: isopleths of (**A**) cloud droplet number concentration (N_{CD}, cm^{-3}), (**B**) activated fraction of aerosol particles (N_{CD}/N, %), and (**C**) maximum water vapor supersaturation (S_{max}, %) calculated as a function of updraft velocity (w, m s^{-1}) and aerosol particle number concentration (N, cm^{-3}). The blue box shows a range of conditions characteristic for pristine Amazonian clouds, the dashed red line indicates the border between the aerosol-limited regime (above line) and the transitional regime (aerosol- and updraft-sensitive, below line)

Table S1. Number concentration, number fraction (relative contribution to total number concentration), and coated fraction (relative proportion with organic coating) of characteristic types of particles measured with various techniques (SEM, UV-APS, DMPS) for different size ranges (submicron, supermicron, total).

Technique	Submicron			Supermicron			Total		
Particle Types	Number concentration	Number fraction	Coated fraction	Number concentration	Number fraction	Coated fraction	Number concentration	Number fraction	Coated fraction
	(cm^{-3})	(%)	(%)	(cm^{-3})	(%)		(cm^{-3})	(%)	(%)
SEM, total	138	100		0.112	100		138	100	
SOA Droplet	117	85		0.002	1.4		117	85	
SOA-Inorganic	13.4	9.7	99.9	0.006	5.6	100	13.4	9.7	99.9
Mineral Dust	0.7	0.5	7.4	0.011	9.5	18.1	0.7	0.5	7.5
Pyro. Carbon	6.7	4.9	54.7	0.001	0.4	100	6.7	4.9	54.7
PBA	0.1	0.1	26.1	0.091	81.1	64.6	0.2	0.2	42.2
Other	0.0	0.0		0.002	2.1		0.0	0.0	
UV-APS, total				0.289	100.0				
FBA				0.114	39.5				
Other				0.175	60.5				
DMPS, total	201	100							
Aitken mode	90	45.0							
Accum. mode	111	55.0							

Table S2. Mass concentration, mass fraction (relative contribution to total mass concentration), and coated fraction (relative proportion with organic coating) of characteristic types of particles and chemical components measured with various techniques (SEM, UV-APS, AMS) for different size ranges (submicron, supermicron, total).

Technique	Submicron			Supermicron			Total		
Particle Types and Components	Mass concentration	Mass fraction	Coated fraction	Mass concentration	Mass fraction	Coated fraction	Mass concentration	Mass fraction	Coated fraction
	($\mu g\ m^{-3}$)	(%)	(%)	($\mu g\ m^{-3}$)	(%)		($\mu g\ m^{-3}$)	(%)	(%)
SEM, total	0.38	100		1.44	100		1.80	100	
SOA Droplet	0.16	43.5		0.01	0.5		0.17	9.6	
SOA-Inorganic	0.12	31.5	99.4	0.05	3.5	100.0	0.17	9.2	99.5
Mineral Dust	0.03	8.7	5.0	0.09	6.3	15.4	0.11	6.2	12.4
Pyro. Carbon	0.05	12.3	69.5	0.00	0.1	100.0	0.05	2.6	70.0
PBA	0.01	3.6	37.3	1.22	84.9	73.5	1.23	68.5	73.1
Other	0.00	0.4		0.07	4.7		0.07	3.8	
UV-APS, total				1.51	100				
FBA				0.98	64.9				
Other				0.53	35.1				
AMS, total	0.56	100							
Organic	0.49	84.5							
Sulfate	0.08	13.7							
Other	0.01	1.7							

Table S3. Number and mass size distribution data ($dN/dlogD$, $dM/dlogD$) as observed by scanning electron microscopy (SEM) and plotted against particle diameter (D) in Fig. 2.

D (μm)	$dN/dlogD$ (cm^{-3})						$dM/dlogD$ (μg m^{-3})					
	SOA	SOA-Inorganic	Mineral Dust	Pyro. Carbon	PBA	Other	SOA	SOA-Inorganic	Mineral Dust	Pyro. Carbon	PBA	Other
0.015	0	0	0	0	0	0	0	0	0	0	0	0
0.025	16.4034	0	0	0	0	0	0.000201	0	0	0	0	0
0.035	108.635	0	0	0	0	0	0.003658	0	0	0	0	0
0.045	141.735	0	0	0	0	0	0.010144	0	0	0	0	0
0.055	234.361	0	0	0	0	0	0.030624	0	0	0	0	0
0.07	188.496	10.2174	0	3.56299	0	0	0.050779	0.002752	0	0.00096	0	0
0.09	115.544	3.98429	0	12.445	0	0	0.066156	0.002281	0	0.007125	0	0
0.11	131.618	14.9654	2.22602	11.5831	0	0	0.137589	0.015644	0.002327	0.012109	0	0
0.14	88.4679	17.0303	0	7.86068	0	0	0.19066	0.036703	0	0.016941	0	0
0.19	62.3748	31.4532	0.69629	16.1425	0	0	0.285704	0.144069	0.003189	0.07394	0	0
0.25	29.1979	25.1379	1.09723	6.73561	0.33571	0.19865	0.358313	0.308488	0.013465	0.082658	0.00412	0.002438
0.35	4.56472	6.48269	0.48282	3.04433	0.00084	0	0.153712	0.218298	0.016258	0.102515	2.81E-05	0
0.45	0.41131	1.13876	0.67078	0.40963	0.30545	0	0.029438	0.0815	0.048007	0.029317	0.021861	0
0.55	0	0.28132	0.69779	0.16282	0.09296	0	0	0.03676	0.09118	0.021275	0.012146	0
0.7	0	0.05898	0.09173	0.10525	0.19347	0.03571	0	0.015888	0.024712	0.028352	0.052119	0.00962
0.9	0	0.07622	0.23691	0	0.05651	0	0	0.043638	0.135644	0	0.032354	0
1.25	0.00263	0.02013	0.01053	0.00277	0.06357	0	0.00403	0.030886	0.016152	0.004246	0.097506	0
2.0	0.00491	0.00997	0.03534	0	0.24205	0.0082	0.030833	0.062657	0.222048	0	1.52082	0.051526
3.0	0	0.00251	0.00573	0	0.13895	0.00158	0	0.053245	0.121614	0	2.94665	0.033547
4.0	0	0.00083	0	0	0.03363	0	0	0.041781	0	0	1.69018	0
5.0	0	0	0.00098	0	0.01229	0.00228	0	0	0.096101	0	1.20624	0.224156
6.0	0	0.00056	0	0	0.00533	0.00066	0	0.094283	0	0	0.905486	0.111382
7.0	0	0.00046	0	0	0.0028	0.00072	0	0.12417	0	0	0.754718	0.193405
8.0	0	0	0	0	0.00079	0.00052	0	0	0	0	0.319357	0.210145
9.0	0	0	0	0	0.00042	0	0	0	0	0	0.24265	0
10.0	0	0	0	0	0	0	0	0	0	0	0	0

Table S4. Number and mass size distribution data (dN/dlog$D$, dM/dlog$D$) as observed by ultraviolet aerodynamic particle sizing (UV-APS) and plotted against particle diameter (D) in Fig. 2.

D (μm)	dN/dlog$D$ (cm^{-3})		dM/dlog$D$ (μg m^{-3})	
	FBA	Other	FBA	Other
1.037	0.002872	0.683472	0.325861	0.001369
1.114	0.004769	0.651753	0.385224	0.002819
1.197	0.007867	0.572229	0.419592	0.005769
1.286	0.012043	0.509111	0.462925	0.01095
1.382	0.022018	0.491761	0.554949	0.024847
1.486	0.042591	0.500151	0.70167	0.059752
1.596	0.070587	0.451371	0.784525	0.122687
1.715	0.143969	0.454485	0.980137	0.310481
1.843	0.225951	0.383867	1.02738	0.604735
1.981	0.292651	0.322684	1.07252	0.972699
2.129	0.373619	0.261604	1.07931	1.54145
2.288	0.465201	0.193139	0.989039	2.38223
2.458	0.487102	0.146599	0.930788	3.09272
2.642	0.419332	0.114451	0.902384	3.30622
2.839	0.278665	0.068808	0.673144	2.72617
3.051	0.20409	0.047883	0.581409	2.47812
3.278	0.175602	0.032039	0.482481	2.64442
3.523	0.159422	0.022291	0.416712	2.98031
3.786	0.098271	0.016219	0.376294	2.28004
4.068	0.065834	0.017467	0.50274	1.89482
4.371	0.039376	0.016164	0.577116	1.40587
4.698	0.023766	0.009225	0.408975	1.05358
5.048	0.011169	0.004699	0.258402	0.61424
5.425	0.004792	0.00217	0.14811	0.327121
5.829	0.001889	0.001022	0.086575	0.159933
6.264	0.001108	0.000679	0.071354	0.116462

6.732	0.000585	0.0005	0.065156	0.076354
7.234	0.000297	0.000484	0.078319	0.048002
7.774	0.000164	0.00025	0.050168	0.032923
8.354	0.000101	0.000265	0.066146	0.025291
8.977	5.46E-05	0.000226	0.070006	0.016898
9.647	7.80E-06	0.000156	0.059917	0.002996
10.37	3.12E-05	0.000203	0.09675	0.014885
11.14	2.34E-05	0.000125	0.07381	0.013839
11.97	7.80E-06	0.000172	0.125906	0.005723
12.86	0	0.000195	0.17742	0
13.82	0	9.37E-05	0.105693	0
14.86	0	0.000101	0.142344	0
15.96	7.80E-06	5.46E-05	0.094959	0.013566
17.15	0	0.000101	0.218815	0
18.43	0	0.00014	0.376001	0
19.81	0	7.02E-05	0.233473	0

Table S5. Number size distribution data (dN/dlog$D$) as observed by scanning mobility particle sizing (SMPS) and plotted against particle diameter (D) in Fig. 2.

D (μm)	dN/dlog$D$ (cm^{-3})
0.021604	47.487
0.024401	75.1253
0.027585	92.2449
0.031192	82.7108
0.035294	94.48
0.039969	128.793
0.045307	171.849
0.051414	210.171
0.058438	259.865
0.066477	307.258
0.075745	319.899
0.0865	287.684
0.099005	233.544
0.113624	223.842
0.130757	277.917
0.150972	312.386
0.175023	300.06
0.203757	178.831
0.238442	99.7828
0.280499	41.9783
0.332025	13.0741
0.395389	3.88362
0.473994	0.652597
0.568793	0.042845
0.682551	0.000915
0.819062	0

Table S6. Mass size distribution data (dM/dlog$D$) as observed by aerosol mass spectrometry (AMS) and plotted against particle diameter (D) in Fig. 2.

D (μm)	dM/dlog$D$ (μg m^{-3})		
	Organic	Sulfate	Other
0.045333	0.020554	0.002435	0.001376
0.051386	0.042286	0.003909	0.001263
0.057767	0.069763	0.005629	0.001169
0.064474	0.101673	0.006944	0.001132
0.071506	0.137663	0.007094	0.001176
0.078859	0.178495	0.005746	0.001293
0.086533	0.225352	0.003476	0.001452
0.094526	0.279287	0.001849	0.0016
0.102839	0.341116	0.002923	0.001676
0.111469	0.411025	0.008389	0.001627
0.120418	0.487356	0.018766	0.001432
0.129684	0.565416	0.033041	0.001133
0.13927	0.637969	0.048936	0.000836
0.149174	0.698012	0.063767	0.00067
0.159398	0.742336	0.075615	0.000723
0.169941	0.773319	0.08423	0.000987
0.180804	0.797597	0.091116	0.001361
0.19199	0.822425	0.098602	0.001713
0.203499	0.851976	0.108447	0.001946
0.215332	0.885365	0.120805	0.002028
0.21117	0.815611	0.110785	-
0.241079	0.883	0.16057	-
0.275223	0.861559	0.154291	-
0.314203	0.684057	0.189019	-
0.358704	0.398284	0.133573	-
0.409507	0.276072	0.09162	-

0.467506	0.330007	0.090849	-
0.53372	0.15256	0.047877	-
0.609311	0.128635	0.044237	-
0.695608	0.102076	0.037008	-
0.794128	0.000182	0.015559	-